UNIVERSITY of York

This is a repository copy of *Insights into the response of coral biomineralisation to environmental change from aragonite precipitations in vitro*.

White Rose Research Online URL for this paper:
https://eprints.whiterose.ac.uk/206603/

Version: Published Version

Article:
Castillo Alvarez, Cristina, Penkman, Kirsty orcid.org/0000-0002-6226-9799, Kröger, Roland orcid.org/0000-0002-5070-0297 et al. (5 more authors) (2024) Insights into the response of coral biomineralisation to environmental change from aragonite precipitations in vitro. Geochimica et Cosmochimica Acta. pp. 184-194. ISSN 0016-7037

https://doi.org/10.1016/j.gca.2023.10.032

Reuse
This article is distributed under the terms of the Creative Commons Attribution (CC BY) licence. This licence allows you to distribute, remix, tweak, and build upon the work, even commercially, as long as you credit the authors for the original work. More information and the full terms of the licence here: https://creativecommons.org/licenses/

Takedown
If you consider content in White Rose Research Online to be in breach of UK law, please notify us by emailing eprints@whiterose.ac.uk including the URL of the record and the reason for the withdrawal request.

White Rose university consortium
Universities of Leeds, Sheffield & York

eprints@whiterose.ac.uk
https://eprints.whiterose.ac.uk/

Geochimica et Cosmochimica Acta 364 (2024) 184–194

Contents lists available at ScienceDirect

Geochimica et Cosmochimica Acta

journal homepage: www.elsevier.com/locate/gca

Insights into the response of coral biomineralisation to environmental change from aragonite precipitations *in vitro*

Cristina Castillo Alvarez [a,b], Kirsty Penkman [c], Roland Kröger [d], Adrian A. Finch [a], Matthieu Clog [e], Alex Brasier [f], John Still [f], Nicola Allison [a,b,*]

[a] School of Earth and Environmental Sciences, University of St. Andrews, St Andrews KY16 9TS, UK
[b] Scottish Oceans Institute, University of St. Andrews, St Andrews KY16 8LB, UK
[c] Department of Chemistry, University of York, York YO10 5DD, UK
[d] Department of Physics, University of York, York, UK
[e] SUERC, University of Glasgow, UK
[f] School of Geosciences, University of Aberdeen, Aberdeen AB24 3UE, UK

ARTICLE INFO

Associate editor: Daniel Sinclair

Keywords:
$CaCO_3$
Coral
Biomineralisation
Aragonite precipitation
Biomolecule

ABSTRACT

Precipitation of marine biogenic $CaCO_3$ minerals occurs at specialist sites, typically with elevated pH and dissolved inorganic carbon, and in the presence of biomolecules which control the nucleation, growth, and morphology of the calcium carbonate structure. Here we explore aragonite precipitation *in vitro* under conditions inferred to occur in tropical coral calcification media under present and future atmospheric CO_2 scenarios. We vary pH, Ω_{Ar} and pCO_2 between experiments to explore how both HCO_3^- and CO_3^{2-} influence precipitation rate and we identify the effects of the three most common amino acids in coral skeletons (aspartic acid, glutamic acid and glycine) on precipitation rate and aragonite morphology. We find that fluid Ω_{Ar} or $[CO_3^{2-}]$ is the main control on precipitation rate at 25 °C, with no significant contribution from HCO_3^- or pH. All amino acids inhibit aragonite precipitation at 0.2–5 mM and the degree of inhibition is inversely correlated with Ω_{Ar} and, in the case of aspartic acid, also inversely correlated with seawater temperature. Aspartic acid inhibits precipitation the most, of the tested amino acids (and generates changes in aragonite morphology) and glycine inhibits precipitation the least. Previous work shows that ocean acidification increases the amino acid content of coral skeletons and probably reduces calcification media Ω_{Ar}, both of which can inhibit aragonite precipitation. This study and previous work shows aragonite precipitation rate is exponentially related to temperature from 10 to 30 °C and small anthropogenic increases in seawater temperature will likely offset the inhibition in precipitation rate predicted to occur due to increased skeletal aspartic acid and reduced calcification media Ω_{Ar} under ocean acidification.

1. Introduction

Biocalcification is the production of calcium carbonate ($CaCO_3$) structures (e.g. shells, plates and skeletons) by a range of organisms. In the marine environment the $CaCO_3$ mineral aragonite is produced by warm and cold-water corals as well as by pteropods and some foraminifera, molluscs and serpulid worms. Biogenic aragonites, including coral skeletons, contain organic molecules, including proteins, glycoproteins and polysaccharides, (Borelli et al., 2003; Cuif et al., 2004; Dauphin 2006; Cuif et al., 2008). These skeletal biomolecules allow calcifying organisms a sophisticated control of mineral crystal nucleation, growth, morphology and physical properties (Addadi and Weiner, 1985; Gilbert et al., 2018). For example, amino acids influence $CaCO_3$ nucleation, growth, morphology and polymorph (Wolf et al., 2007; Picker et al., 2012; Montanari et al., 2016; Stepić et al., 2020; Fang et al., 2023).

The main physico-chemical parameters controlling the precipitation rates of $CaCO_3$ minerals are the degree of supersaturation of fluid, the temperature and the presence of additives (Berner, 1975; Mucci and Morse, 1984; Burton and Walter, 1987; de Yoreo and Vekilov, 2003; Morse et al., 2007; Nielsen et al., 2013). The $CaCO_3$ saturation state of seawater (Ω) is a function of the $[Ca^{2+}]$, $[CO_3^{2-}]$ and K_{sp}, which is the

* Correspondence author.
E-mail address: na9@st-andrews.ac.uk (N. Allison).

https://doi.org/10.1016/j.gca.2023.10.032
Received 6 January 2023; Accepted 27 October 2023
Available online 29 October 2023
0016-7037/© 2023 The Authors. Published by Elsevier Ltd. This is an open access article under the CC BY license (http://creativecommons.org/licenses/by/4.0/).

solubility product at a given temperature, salinity and pressure and is mineral specific (Mucci, 1983). However, it is unclear if HCO_3^- also plays a role in $CaCO_3$ precipitation (Wolthers et al., 2012; van der Weijden and van der Weijden, 2014; Andersson et al., 2016; Sand et al., 2016; De Carlo et al., 2018).

Coral aragonite is deposited at an extracellular calcification site at the base of the coral and is either precipitated from ions in the extracellular calcification media or sourced from amorphous $CaCO_3$ formed intracellularly in vesicles in the calicoblastic cells overlying the extracellular site (Sun et al., 2020). The coral calcification media are at least semi-isolated from seawater and have elevated pH, favouring the speciation of CO_3^{2-} (Al Horani et al., 2003, Venn et al., 2019). Ocean acidification can reduce the pH of both the calicoblastic cell intracellular fluid and the extracellular calcification media (Venn et al., 2013), influencing fluid/media DIC speciation and the relative proportions of aqueous HCO_3^- and CO_3^{2-}. In addition, the biomolecule concentrations of tropical coral skeletons are increased by ocean acidification (Tambutté et al., 2015; Kellock et al., 2020). Understanding how these changes influence aragonite precipitation rate is crucial to predicting the future of coral reef accretion.

In this research we explore aragonite precipitation *in vitro* under conditions reflective of the coral calcification media over a range of Ω_{Ar} values. We precipitate aragonite onto a seed using a specialist apparatus designed to maintain pH, Ω_{Ar} and $[Ca^{2+}]$ within narrow limits (Kellock et al., 2020). We vary pH, Ω_{Ar} and pCO_2 between experiments to explore how both HCO_3^- and CO_3^{2-} influence precipitation rate, and we test the impact of the three most abundant amino acids in coral skeletons (aspartic acid, glutamic acid and glycine, Kellock et al., 2020) on aragonite precipitation. These amino acids are common in the skeletal organic matrix of other calcareous organisms (Weiner, 1979; Weiner and Addadi, 1991; Takeuchi et al., 2008; Suzuki et al., 2009; Rahman et al., 2013). We also explore the role of temperature in precipitation rate, both in the presence and absence of aspartic acid. We use these experiments to hypothesise how future environmental change may affect aragonite precipitation *in vivo*.

2. Methods

2.1. Aragonite precipitations

We precipitated aragonite from artificial seawater at 25 °C unless otherwise stated. To decouple the effect of pH and Ω_{Ar} on aragonite precipitation rate, experiments were conducted at constant Ω_{Ar} (of 4, 7, 10, 13 or 18) and with variable pH_{NBS} (8.337, 8.545 or 8.727). Repeat precipitations were conducted 3 to 4 times under each set of conditions. The NBS (National Bureau of Standards) pH scale is used for pH measurements calibrated with pH buffer solutions. The pH_{NBS} and Ω_{Ar} of the extracellular calcification media of corals cultured at present day pCO_2 are ~8.5 and ~11 based on microsensor and fluorescent dye measurements (Sevilgen et al., 2019). This is in good agreement with calcification media pH_{NBS} estimates from $\delta^{11}B$ analyses of coral skeletons cultured at 400 µatm seawater pCO_2 (pH = 8.5–8.6; Allison et al., 2018, 2021). Fluorescent dye and $\delta^{11}B$ measurements suggest that decreasing seawater pH from 8.0 to 7.8 (consistent with an increase of seawater pCO_2 from ~400 to 750 µatm) can reduce calcification media pH by up to ~0.2 pH units in some (Venn et al., 2013, 2022; Holcomb et al., 2014; Allison et al., 2021) but not all coral individuals (Allison et al., 2018, 2021).

To explore the effects of amino acids on aragonite precipitation, multiple experiments were conducted at $\Omega_{Ar} = 13$, $pH_{NBS} = 8.474$ and $pCO_2 = \sim 410$ µatm with the addition of 0.2, 1.0, 2.0, 3.0 or 5.0 mM of amino acid (aspartic acid, glycine or glutamic acid). These experiments were not duplicated. Comparing the aspartic acid contents of synthetic aragonites precipitated at known seawater [aspartic acid] with coral skeletons suggests that the [aspartic acid] of the coral calcification media is ~0.1–0.4 mM (Kellock et al., 2020). To test how the effect of amino acids on aragonite precipitation is influenced by pH and Ω_{Ar} we precipitated aragonite at variable Ω_{Ar} and pH as before, but this time in the presence of 2 mM aspartic acid, glycine or glutamic acid. Repeat precipitations were conducted 3 to 4 times under each set of conditions as before. Finally, to study how temperature and biomolecules interact, precipitations were performed between 10 and 30 °C at 5 °C increments at $\Omega = 14$ and $pCO_2 = 410$ µatm in the absence and presence of 1 mM aspartic acid. Experiments were completed 1 to 3 times under each set of conditions.

2.1.1. Precipitation apparatus

Aragonites were precipitated from artificial seawater using the constant composition method (Beck et al., 2013) and described in detail in Kellock et al., (2020, 2022). In short, the dissolved inorganic carbon (DIC) and pH of the seawater were adjusted to predefined values in a precipitation apparatus and an aragonite seed was added to provide a surface for aragonite growth (Kellock et al., 2022). The pH of the solution was constantly monitored using a high precision pH/temperature sensor (Metrohm Aquatrode Pt1000). $CaCO_3$ precipitation reduces seawater pH and this decrease triggers the addition of equal volumes of 2 titrants (0.45 M Na_2CO_3 and 0.45 M $CaCl_2$ and $SrCl_2$ in a 99:1 ratio) from an adapted Metrohm Titrando 902 titrator to replace the ions consumed in precipitation. The second titrant contains a mixture of Ca and Sr to reflect the substitution of Sr for Ca into the aragonite (Finch et al., 2003).

Experimental beakers were immersed in a water bath (Grant Instruments 120 TC) set at the desired temperature. All experiments, aside from the temperature dependent subset, were conducted at T = 25 °C. For experiments below 25 °C, a cooler (Grant Instruments CG1) was inserted into the water bath to maintain the set temperature. Beakers were capped with an ethylene tetrafluoroethylene lid with ports through which the pH/temperature sensor, a propeller stirrer, a gas tube and the 2 titrant dosing tubes were inserted.

The pCO_2 of the experimental seawater was maintained by bubbling it with an airstream (at ~10 mL min^{-1}) with the CO_2 adjusted to be in equilibrium with the seawater. For ambient pCO_2 experiments (CO_2 = ~410 ppm), air was sourced from outside the building and warmed before use. Above ambient CO_2 airstreams were produced by combining ambient air with high purity CO_2 using high precision mass flow controllers (SmartTrak 50 Series, Sierra USA). Below ambient CO_2 airstreams were produced by flowing ambient air through NaOH pellets to remove CO_2 and then combining this with high purity CO_2 as before. Airstream $[CO_2]$ was determined using an infrared CO_2 analyser (WMA04, PP systems, USA).

2.1.2. Experimental procedure

Artificial seawater for the experiments was prepared following the composition described in Millero (2013) and had a salinity of 35. It was stored in a blacked-out 100L container and filtered through a 0.2 µm polyether sulfone filter before use. The aragonite seed was obtained by grinding a coral skeleton in an agate ball mill and had a surface area of 4.27 ± 0.11 m^2g^{-1} (1σ, n = 3) as analysed by the Brunauer–Emmett–Teller technique (Brunauer et al., 1938).

For each precipitation, 340 mL of artificial seawater previously equilibrated with ambient air was placed in a HDPE plastic beaker. Seawater DIC was elevated by the addition of 0.6 M Na_2CO_3 and pH was adjusted by addition of 2 M HCl and sometimes NaOH. A few minutes were allowed for the solution pH to stabilize and then the software controlling the titration was initiated and 200 mg of seed was introduced into the vessel. In all experiments 300 mg of aragonite was precipitated (i.e. 6.7mLs of each titrant were dosed). A sample titration is illustrated in Fig. 1. showing the typical pH control during experiments. Synthetic amino acids, when used, were sourced from Sigma-Aldrich (purity ≥ 99 %) and were dissolved in 1.5 mL of seawater and added to the titration vessel before the addition of Na_2CO_3. At the end of each titration, solids were recovered by passing the solution through a 0.2 µm polycarbonate

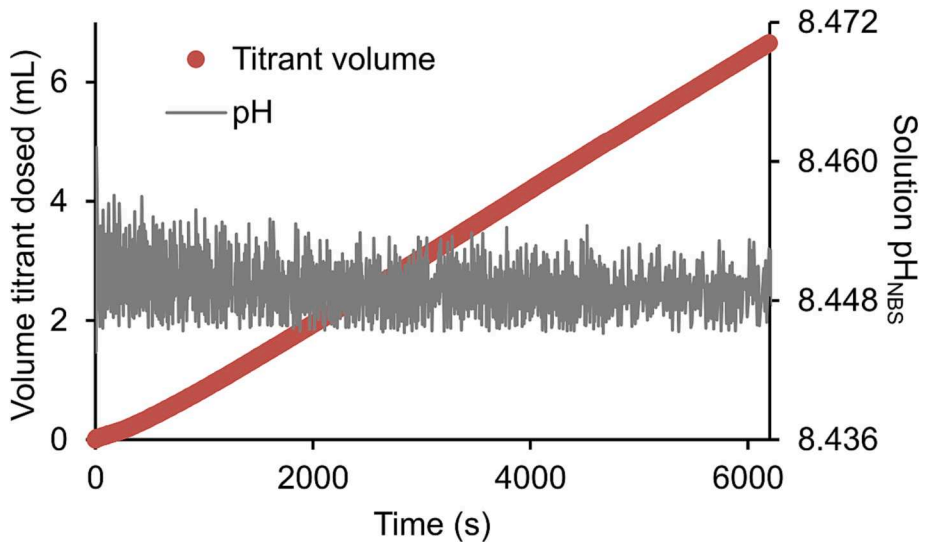

Fig. 1. Typical titration curve showing volume of titrant dosed over time and the pH of seawater throughout the experiment.

filter (Nucleopore). The aragonite was rinsed with deionised water (18.2 Megaohm milli-Q) and ethanol and dried at room temperature.

2.1.3. DIC chemistry characterisation

The pH sensor was calibrated with fresh NIST (National Institute of Standards and Technology) buffers weekly and pH is reported on the NBS scale. The maximum change in buffer pH between one week and the next was 0.004 pH units. The total alkalinity of artificial seawater batches was characterised by automated Gran titration (Metrohm, 888 Titrando) with a typical precision of $\pm$ 2 μeq kg^{-1} (1 s, Cole et al., 2016) and varied from 2192 to 2280 μmol kg^{-1} between seawater batches. Seawater [DIC] was measured at the start and end of each experiment using a CO_2 differential, non-dispersive, infrared gas analyser (Apollo SciTech; AS-C3) with the exception of the temperature experiments where one replicate was measured for each set of conditions. The DIC analyser was maintained in a temperature-controlled room at 20 °C and calibrated weekly using a natural seawater certified reference material (CRM 171, Scripps Institution of Oceanography) as in Cole et al, 2016. Changes in the DIC calibration between adjacent weeks were assessed by processing the standard data from the first week using the calibration of the second week and equated to $\leq$7 μmol kg^{-1} on a sample of 4000 μmol kg^{-1}. We consider drift in the DIC analyser over the course of a week to be insignificant.

The pH$_{NBS}$ and mean DIC of the solutions were used to calculate Ω_{Ar} using CO_2 Sys v2.1 (Pierrot et al., 2006) with the equilibrium constants for carbonic acid and $KHSO_4$ from Lueker et al. (2000) and Dickson (1990) respectively and seawater [B] from Lee et al. (2010). Temperature was set to the measured value and salinity to 35 (assuming a [Ca^{2+}] of 10.27 mM). DIC typically varied by <5 % over a precipitation, equivalent to a change in Ω of ~0.5 at Ω = 7 and ~1.0 at Ω = 18.

2.2. Precipitate characterisation

The precipitation rate (R_p) of the aragonite overgrowths was obtained by calculating the rate of titrant addition (from a linear fit between time and volume of titrant dosed as in Fig. 1) and was normalising to the surface area of the starting seed (Kellock et al., 2022).

We used Raman spectroscopy to confirm the $CaCO_3$ polymorph of all the precipitates. Raman spectra of the precipitates and the original seed were collected between 100 and 1311 wave numbers with a Renishaw In-Via Qontor Raman Microscope using a NIR 300 mW 785 nm solid state laser set at 5 % full power and with a 1200 cm^{-1} grating. The laser spot was focused onto the edges of the aragonite particles and data were collected for 2 s. 10 to 12 particles were tested for each aragonite. These conditions were selected after testing a range of laser powers and times and optimised the signal:noise of the samples (Supplementary Fig. 1). All the Raman spectra had lattice mode peaks at ~153 and 206 cm^{-1} (De Carlo 2018) and a doublet v_4 peak (Urmos et al., 1991), indicative of aragonite. Repeating analyses on the same spot >100 times did not affect the presence of these peaks and we consider that no transformation of the mineral occurred during analysis. We did not analyse the full width half maxima of the v_1 peak of the Raman spectra which has been reported previously to relate to precipitating fluid Ω_{Ar} (De Carlo et al., 2017).

Scanning electron micrograph (SEM) images were collected of select precipitates. Precipitates were mounted on aluminium pin stubs (25 mm diameter) using double-sided carbon adhesive discs and carbon-coated twice under vacuum (Quorum K950 carbon coater), rotating the samples 90° between coats to ensure full coverage. Samples were viewed using a CarlZeiss GeminiSEM 300 (ACEMAC Facility, University of Aberdeen) using an accelerating voltage of 2.5 keV and an InLens secondary electron detector.

3. Results

3.1. Effects of CO_3^{2-} and HCO_3^- on aragonite precipitation without biomolecules

Precipitation rate shows strong linear positive correlations with both Ω_{Ar} and [CO_3^{2-}] (Fig. 2a) but relationships with [HCO_3^-] and pH are more complicated (Fig. 2 b and c). Multiple linear regression analysis of precipitation rate versus [CO_3^{2-}], [HCO_3^-] and pH indicates that aragonite precipitation rate is significantly positively correlated with [CO_3^{2-}] but not with [HCO_3^-] or pH (Table 1, p values = 2.7 × 10^{-26}, 0.75, 0.58 respectively).

3.2. Effects of amino acids on aragonite precipitation

All the amino acids supressed aragonite precipitation at all the concentrations tested compared to the experiments with no biomolecule (Fig. 3). The % inhibition was calculated from the precipitation rate with biomolecule compared to the aragonite precipitation rate at the same pH and Ω_{Ar} with no biomolecule. Aspartic acid had the greatest inhibitory effect, followed by glutamic acid and then glycine. The degree of inhibition plateaued above ~2 mM with glutamic acid and above ~1 mM with glycine but no plateau is observed in our experiments with aspartic

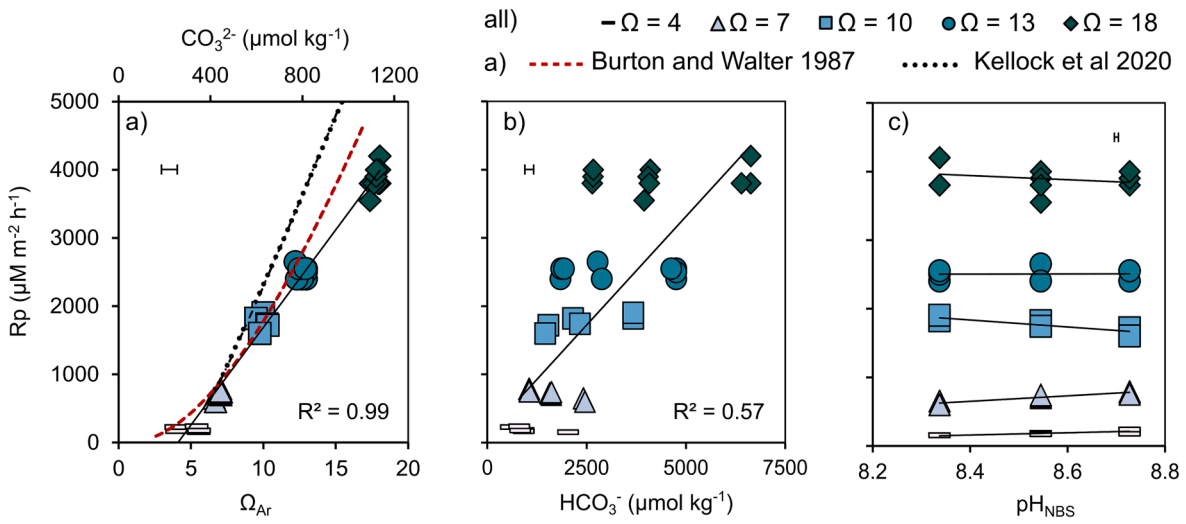

Fig. 2. Aragonite precipitation rates without biomolecules (R_p) at 25 °C plotted as a function of a) Ω_{Ar} and $[CO_3^{2-}]$, b) $[HCO_3^-]$ and c) pH. Typical errors in pH_{NBS}, Ω and $[HCO_3^-]$ are superimposed onto each graph. pH uncertainty is estimated from the maximum drift in sensor pH observed over a week (0.004 units) and Ω and $[HCO_3^-]$ uncertainties are estimated by compounding the typical change in DIC over the course of a titration (<5%) with the maximum pH drift observed (0.004 pH units) to yield Ω and $[HCO_3^-]$ uncertainties of 0.5 and 125 μmol kg^{-1} at Ω = 7 and 1.1 and 205 μmol kg^{-1} at Ω = 18. Error bars show the largest uncertainties and are smaller than the symbols used. We do not calculate uncertainty on precipitation rate within a titration as we repeat multiple titrations for each of conditions and the range of points shows the variations between experiments. Precipitation rates from duplicate experiments typically agree within 5 %. Inorganic aragonite precipitation rates at 25 °C in natural seawater from Burton and Walter, 1987 and Kellock et al., 2020 are superimposed onto a). Linear relationships between precipitation rate and Ω and $[HCO_3^-]$ are shown by single lines in a) and b) with coefficients of determination (r^2). Relationships between precipitation rate and pH are shown for each Ω in c).

Table 1
Summary of p values generated in statistical tests in this study. We use multiple linear regression analyses to determine if $[CO_3^{2-}]$, $[HCO_3^-]$ and pH influence aragonite precipitation rate and if Ω_{Ar} and pH influence the % inhibition of aragonite precipitation rate by amino acids. We use one-way ANCOVA tests to compare linear relationships between aragonite precipitation rates as a function of Ω_{Ar} or temperature between treatments. p values ≤ 0.05 are highlighted in bold.

Multiple linear regression tests			
Influence of $[CO_3^{2-}]$, $[HCO_3^-]$ and pH on aragonite precipitation rate, 25 °C (Fig. 2)	CO_3^{2-}	HCO_3^-	pH
	2.7×10^{-26}	0.75	0.58
Influence of Ω and pH on % inhibition of aragonite precipitation (Fig. 6)	Ω_{Ar}	pH	
2 mM aspartic acid, 25 °C	**9.3×10^{-12}**	0.18	
2 mM glycine, 25 °C	**4.0×10^{-6}**	0.42	
2 mM glutamic acid, 25 °C	**2.1×10^{-13}**	**0.010**	
ANCOVA tests	p (equal means)	p (equal slopes)	
Ω vs aragonite precipitation rate, 25 °C (Fig. 4)			
2 mM aspartic acid compared to no amino acid	**4.2×10^{-26}**	**1.7×10^{-20}**	
2 mM glycine compared to no amino acid	**2.3×10^{-19}**	**0.20**	
2 mM glutamic acid compared to no amino acid	**3.1×10^{-26}**	**0.76**	
Ω vs % inhibition of aragonite precipitation rate, 25 °C (Fig. 5)			
2 mM aspartic acid compared to 2 mM glycine	**2.6×10^{-28}**	0.48	
2 mM aspartic acid compared to 2 mM glutamic acid	**9.0×10^{-22}**	**0.014**	
2 mM glycine compared to 2 mM glutamic acid	**1.2×10^{-6}**	0.18	
Temperature vs log aragonite precipitation rate, Ω = 13 (Fig. 7b)			
1 mM aspartic acid compared to no amino acid	**3.1×10^{-6}**	0.61	

acid (up to 5 mM).

Aragonite precipitation rates in the presence of 2 mM aspartic acid, glycine or glutamic acid are strongly positively correlated with Ω_{Ar} but are slower without biomolecules for comparable Ω_{Ar} (Fig. 4). Both the mean (testing the mean precipitation rate at set Ω) and slope of the relationships between Ω_{Ar} and precipitation rate are significantly different in the presence of aspartic acid while the mean relationships are affected by the presence of glycine and glutamic acid (ANCOVA, Table 1).

The % inhibition of aragonite precipitation in the presence of 2 mM amino acid was calculated from the precipitation rate with biomolecule compared to the aragonite precipitation rate at the same Ω_{Ar} with no biomolecule (Fig. 5). Aspartic acid had the greatest inhibitory effect on precipitation of all the tested amino acids while glycine had the least and inhibition was highest at low Ω_{Ar} for all amino acids. Relationships between Ω_{Ar} and aragonite precipitation inhibition are significantly different between all amino acids (ANCOVA, Table 1) with the exception that slopes between Ω_{Ar} and aragonite precipitation inhibition by amino acid are not signficantly different between aspartic acid and glycine.

At constant pCO_2, both pH and Ω covary. We conducted experiments under varying pH and pCO_2 (as in Kellock et al., 2020) to decouple the influences of pH and Ω_{Ar} on inhibition of aragonite by amino acids (Fig. 6). We used multiple linear regression analysis to test the effects of pH and Ω_{Ar} on aragonite inhibition (Table 1). Ω_{Ar} significantly influenced the degree inhibition of precipitation by all amino acids (with inhibition highest at low ΩAr, Fig. 6). pH also significantly affected the degree of inhibition in the presence of glutamic acid (with inhibition highest at low pH, Fig. 6).

3.3. Temperature

Temperature and aragonite precipitation rates are positively related by exponential functions both in the absence and presence of 1 mM aspartic acid (Fig. 7a). After converting precipitation rates to a log scale to produce linear relationships between temperature and aragonite precipitation rates (Fig. 7b), ANCOVA analysis indicates that aragonite precipitation rates were significantly slower with the aspartic acid, although the slope of the 2 relationships was not significantly different (Table 1). The degree of aragonite precipitation inhibition was higher at low temperatures (Fig. 7c).

3.4. Characterisation of precipitates

We identify all precipitates as aragonite based on the observation of lattice mode peaks at ~153 and 206 cm^{-1} (De Carlo 2018) and on the

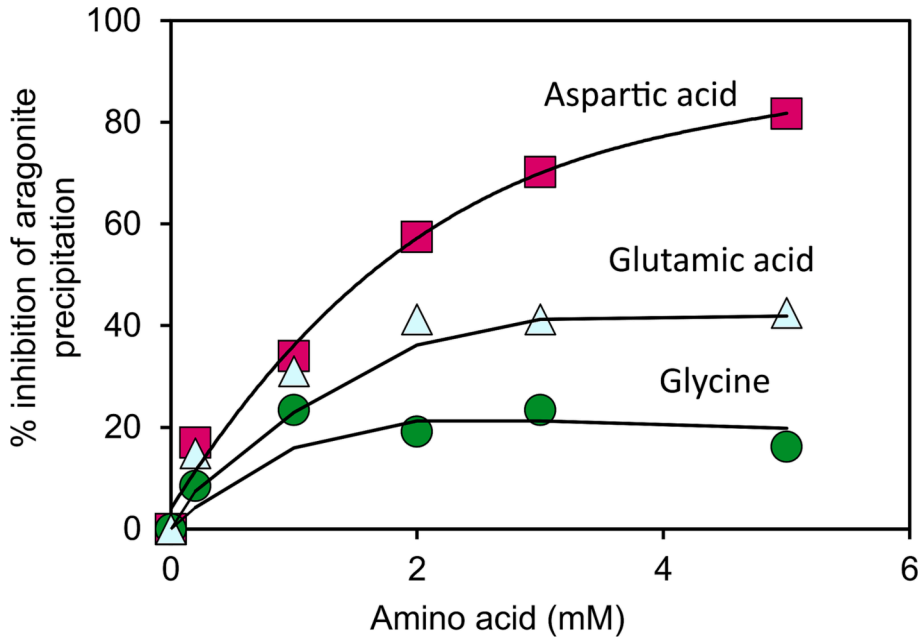

Fig. 3. Inhibition of aragonite precipitation rate by aspartic acid, glycine and glutamic acid at $\Omega_{Ar} = 13$ and $pH_{NBS} = 8.474$. These experiments were not duplicated and no uncertainties are shown. Precipitation rates in other duplicated experiments typically agree within 5 %.

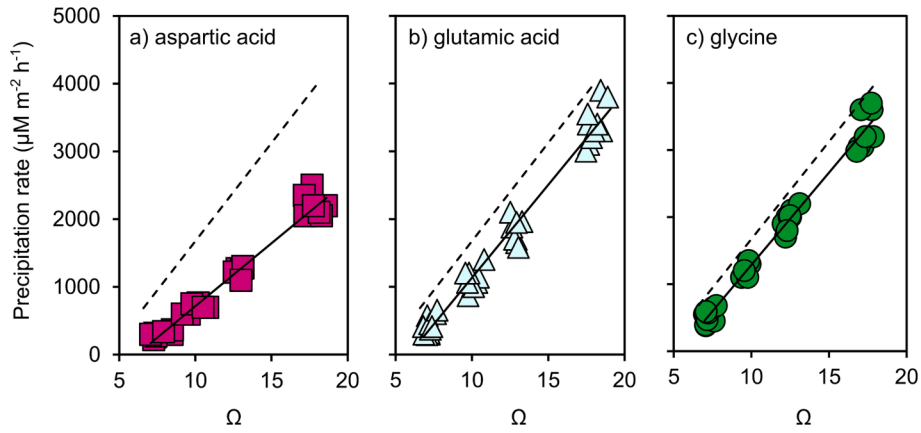

Fig. 4. Precipitation rate as a function of seawater Ω_{Ar} for experiments with the addition of 2 mM: a) aspartic acid, b) glutamic acid, and c) glycine. Solid black lines show linear best fit lines and coefficients of determination (r^2) are 0.98 for each relationship. The dotted black line indicates the linear regression obtained from experiments without amino acids (Fig. 2a). Variation in [DIC] within each precipitation and uncertainty in pH compound to yield Ω uncertainty of up to 1.1 at high Ω which is smaller than the symbols used (see legend to Fig. 2). Multiple precipitations are shown under each set of conditions to indicate uncertainty in precipitation rate.

dual peak (v_4) between 700 and 710 cm^{-1} in the Raman spectra (Urmos et al., 1991). We explore the morphology of select precipitates by SEM (Fig. 8). A pyramidal crystal morphology is observed in all the aragonite overgrowths examined (Fig. 8b–e). Multiple pyramidal crystals are observed, often radiating in different directions from a common point. The crystals exhibit roughened surfaces suggesting that they are composed of nano-particles typically 100–200 nm in dimensions. The crystal surfaces can be studded with further small crystallites (yellow arrows in Fig. 8). Aragonites produced in the presence of aspartic acid (Fig. 8d) have pointier pyramids than aragonite produced with glycine, glutamic acid and no biomolecule.

4. Discussion

4.1. Roles of HCO_3^- and CO_3^{2-} in aragonite precipitation

Aragonite precipitation rate without biomolecules is linearly related to $[CO_3^{2-}]$ and Ω_{Ar} (a measure of seawater $[CO_3^{2-}]$) and $[HCO_3^-]$ has no significant effect on precipitation rate over the range of Ω tested (Table 1). Research on the roles of CO_3^{2-} and HCO_3^- in $CaCO_3$ precipitation has focused predominantly on calcite. HCO_3^- was inferred to attach to growing calcite crystal surfaces (Wolthers et al., 2012), thereby contributing to calcite growth (Christoffersen and Christoffersen, 1990; van der Weijden et al., 1997; van der Weijden and van der Weijden, 2014). However, density theory function modelling indicates that HCO_3^- is relatively unstable when adsorbed to calcite faces and is likely to deprotonate (Andersson et al., 2016). A complete understanding of calcite growth kinetics remains elusive (Sand et al., 2016) but these latter findings suggested that HCO_3^- plays little role in calcite precipitation. Although $[HCO_3^-]$ does not influence aragonite precipitation rate in the present study, the HCO_3^- species has been detected in both coral skeletons and synthetic aragonite (Von Euw et al., 2017). Our data show that large changes in $[HCO_3^-]$ (e.g. x3; Fig. 2) are not associated with changes in aragonite precipitation rate, suggesting that any role in

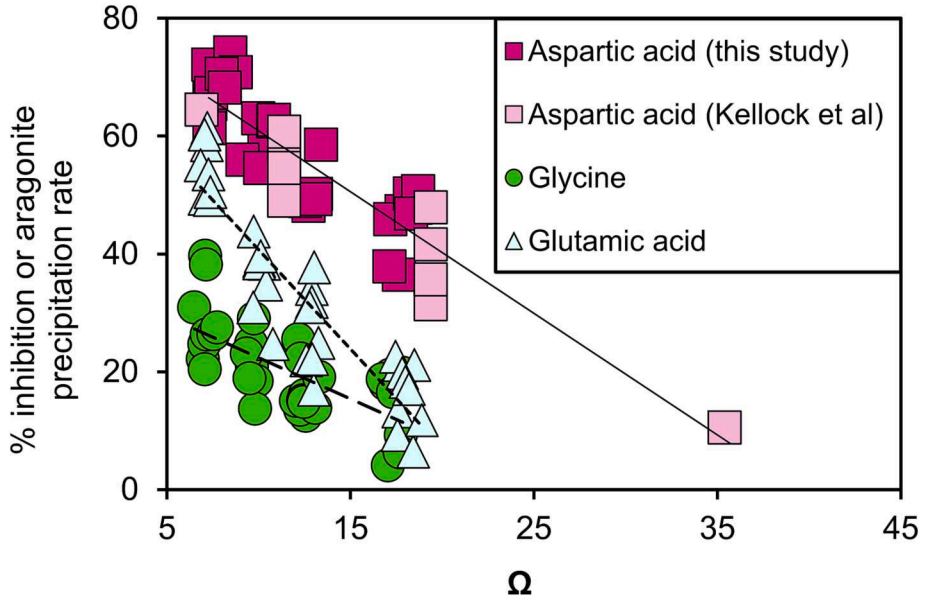

Fig. 5. Inhibition of aragonite precipitation rates by amino acids (2 mM) as a function of Ω_{Ar}. We include the data from Kellock et al., (2020) which also measured inhibition of aragonite precipitation by 2 mM aspartic acid. Uncertainty in Ω is smaller than the symbols used (see legend to Fig. 2) and multiple precipitations are shown under each set of conditions to indicate uncertainty in inhibition of precipitation rate.

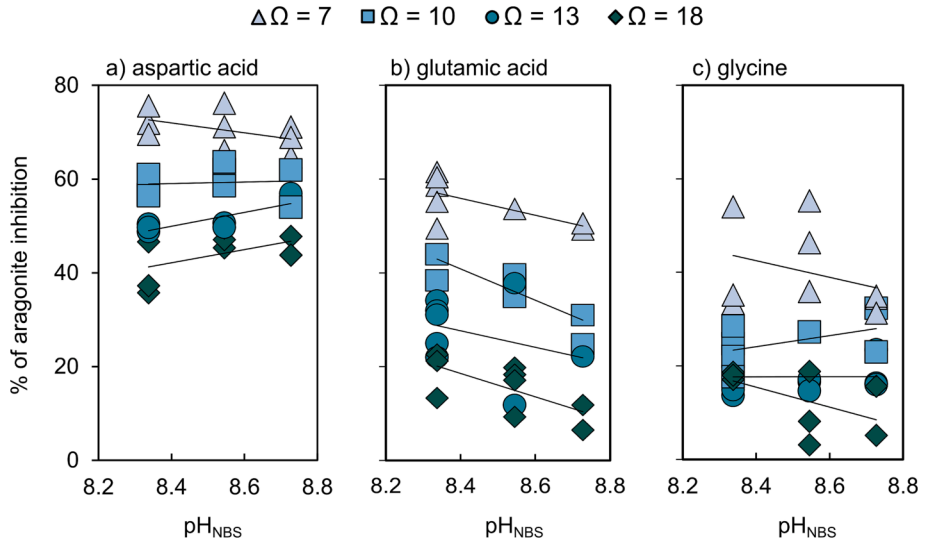

Fig. 6. Inhibition of aragonite precipitation by the addition of 2 mM a) aspartic acid, b) glutamic acid, and c) glycine as a function of pH and Ω_{Ar}. Uncertainty in pH is <0.004 pH units (smaller than the symbols used). Multiple precipitations are shown under each set of conditions to indicate uncertainty in inhibition of precipitation rate.

aragonite precipitation is minor.

Aragonite precipitation rates in seawater are exponentially related to Ω over a broader Ω range than explored in the present study (Burton and Walter, 1987; Kellock et al., 2020). Precipitation rates with no biomolecules in the present study (in artificial seawater) are in good agreement with previous reports in natural seawater at low Ω but are slower than previous reports at higher Ω (Fig. 2a, Burton and Walter 1987; Kellock et al., 2022). Similarly, precipitation rates at Ω = 14 over a range of temperature in the present study are lower than estimated from precipitation in natural seawater (Fig. 7b, Burton and Walter, 1987). Aragonite precipitation rates were significantly slower in artificial seawater compared to natural seawater suggesting that the dissolved organic matter in natural seawater may promote $CaCO_3$ precipitation (Kellock et al., 2020). We do not include the aragonite precipitation rates observed in NaCl solutions (Mavromatis et al., 2015) as $[Mg^{2+}]$ (a known inhibitor of $CaCO_3$ precipitation, Pan et al., 2021) is presumably much lower in these solutions than in seawater.

De Carlo et al., (2015) and Holcomb et al., (2016) also precipitated aragonites from seawater over a broad range of DIC conditions. Precipitation rates are difficult to characterise in these studies as the $[Ca^{2+}]$ consumed during precipitation was not replaced in the experiments, resulting in large changes in solution $[Ca^{2+}]$ (4 to 47 % in De Carlo et al., 2015 and 17 to 71 % in Holcomb et al., 2016). These changes affect Ω_{Ar} and are likely to influence $CaCO_3$ precipitation rate within each precipitation. In addition, seeds were not typically used in these 2 previous studies. Unseeded aragonite precipitations in seawater can be highly variable in duration and do not provide reproducible estimates of precipitation rate in repeat experiments, suggesting that the aragonite surface area nucleated at the start of precipitation is inconsistent between experiments (Kellock et al., 2022). Precipitation rates become

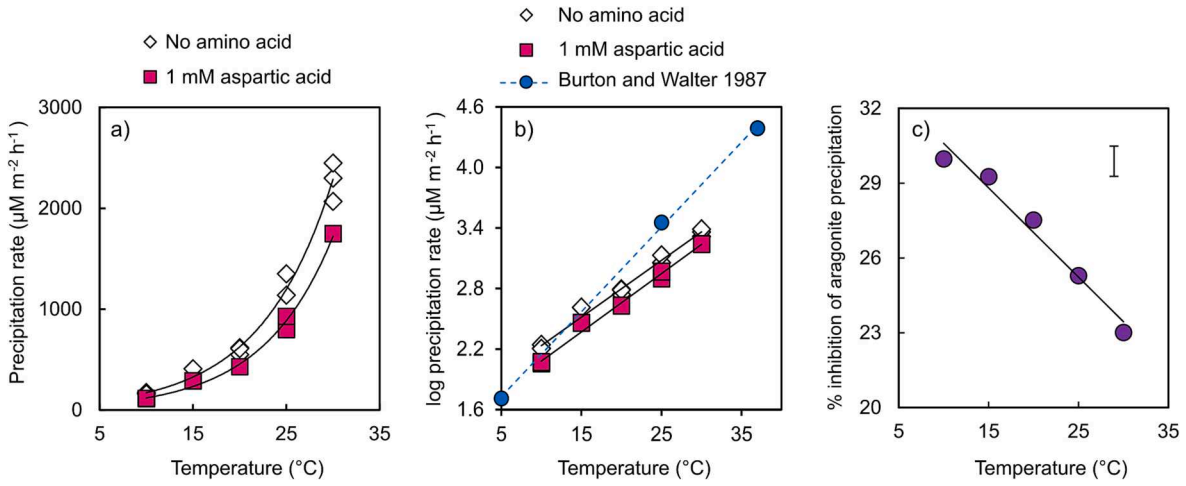

Fig. 7. a) and b) aragonite precipitation rate as a function of temperature without amino acids and with the addition of 1 mM aspartic acid. The maximum difference in temperature recorded by the pH sensor within each precipitation was 0.026 °C and is insignificant in comparison with the size of the symbols used. Multiple precipitations are shown under each set of conditions in a) and b) to indicate uncertainty in precipitation rate. Inorganic aragonite precipitation rates at $\Omega = 14$ are estimated from experiments conducted at 5, 25 and 37 °C in natural seawater (Burton and Walter, 1987) and are superimposed onto b). c) The percentage reduction in precipitation rate after addition of 1 mM aspartic acid as a function of temperature in this study. In c) the floating error bar reflects the uncertainty calculated by compounding the variability in precipitation rates with and without aspartic acid to calculate uncertainty on the % inhibition of precipitation rate. Different symbols are used in c) as this data reflects a combination of data from precipitations with and without aspartic acid.

reproducible when sufficient seed of known surface area is provided and used to normalise aragonite precipitation rate (Kellock et al., 2022).

4.2. The effects of amino acids on aragonite precipitation rate

All the amino acids suppressed aragonite precipitation at 0.2–5 mM. Aspartic acid concentrations of 1 mM or higher inhibited aragonite precipitation from seawater while concentrations of 1–10 μM promoted aragonite formation in a previous study (Kellock et al., 2022). Additives can influence $CaCO_3$ formation by either binding the aqueous ions involved in mineralisation (Ca^{2+} or CO_3^{2-}) or by interacting directly during $CaCO_3$ nucleation or growth (i.e. by influencing the formation of soluble pre nucleation clusters, inhibiting nucleation or by adsorbing to nucleated particles, Gebauer et al., 2009). Organic additives, including amino acids, may slow mineral growth by adsorbing to the crystal surface and blocking the attachment of other ions (Sikirić and Füredi-Milhofer, 2006) or promote growth by decreasing the energy barrier to ion attachment (Elhadj et al., 2006). Organic additives have also been found to stabilize calcium (bi)carbonate networks and hinder their transformation into solid $CaCO_3$ (Finney et al., 2020). Aspartic and glutamic acid are the only amino acids that have negatively charged side chains (caused by the deprotonation of the COOH groups to the left of each image in Fig. 9). These amino acids are capable of cation binding and form metal complexes in seawater (de Stefano et al., 1995). Glycine does not have a side chain (Fig. 9) but is also reported to bind Ca^{2+} and Mg^{2+} (de Stefano et al., 1995). Aspartic acid speciation in artificial seawater is dominated by Na^+, Mg^{2+} and Ca^{2+} complexes and over the pH range 8 to 9, $Ca(Asp)H^+$ and $Ca(Asp)^0$ bind ~10 % of the aspartic acid (de Stefano et al., 1995). If similar binding occurs in our experiments, then the addition of 2 mM aspartic acid results in ~0.2 mM of Ca^{2+} forming complexes with the aspartic acid and reduces Ω by ~0.2 at $\Omega = 11$ and ~0.4 at $\Omega = 19$. The precipitation rate of aragonite at $\Omega = 11$ in the presence of 2 mM aspartic acid is ~58 % of the rate observed with no amino acid (Fig. 5), i.e. equivalent to that observed at $\Omega = 7$ with no amino acid (Fig. 4). This is a much higher reduction that anticipated from the binding of Ca by the amino acid alone and indicates that the mechanism by which aspartic acid influences aragonite precipitation is more complex that simply binding Ca^{2+}. Amino acids may influence $CaCO_3$ formation in several further ways. All the amino acids tested here are reported to retard $CaCO_3$ nucleation, aspartic and glutamic acids can stabilise $CaCO_3$ prenucleation clusters and both aspartic acid and glycine can increase the solubility of the initially precipitated $CaCO_3$ phase (Picker et al., 2012).

Although aspartic and glutamic acids are structurally very similar, we find pronounced differences in the ways they influence precipitation. In the present study aspartic acid caused the highest degree of inhibition of aragonite precipitation but glutamic acid displayed the largest variation in degree of inhibition over varying Ω (Fig. 5). Poly-peptides of aspartic acid have a greater influence on the morphology of calcium oxalate crystals compared to polyglutamates (Guo et al., 2002, Jung et al., 2005). Molecular dynamics simulations of the behaviour of penta-aspartic and penta-glutamic acids suggest that Ca^{2+} associates more closely with the penta-aspartic acid, promoting mineralisation (Lemke et al., 2021). The shorter aspartic acid side chains could increase the density of binding sites in the molecule (the binding site spacing hypothesis) or could facilitate the binding of divalent cations by multiple COO^- groups on the peptide surface (Lemke et al., 2021). Single residue aspartic and glutamic acids also behave differently in some early stages of $CaCO_3$ crystallisation (Picker et al., 2012) but the reason for this is less clear. Acidic amino acids adsorb onto aragonite (Kawano and Tokonami, 2014) and the sidechain length may affect how adsorbed amino acids interact with ions involved in precipitation. Alternatively, amino acids themselves can form prenucleation clusters in solution (Kellermeier et al., 2012) and the length of the acidic side chain may influence the interaction of such clusters with mineralisation ions.

Inhibition of aragonite precipitation rate by amino acid was higher at low Ω (all amino acids) but was also affected by pH for glutamic acid (less inhibition at high pH). Inhibition of aragonite precipitation rate by aspartic acid was also higher at low temperatures. In all cases higher inhibition was observed in the experiments with the lowest aragonite precipitation rates. This observation could be explained if amino acid adsorption to the aragonites is reduced at high precipitation rates (see Kellock et al. 2020 for a discussion of this).

4.3. Aragonite morphologies

All the aragonite overgrowths exhibit pyramidal crystals which typically extend in different directions from a common point (the site of nucleation) and reach ~1 μm in length (Fig. 8b–e). The pyramidal crystals exhibit roughened surfaces suggesting that they are composed of

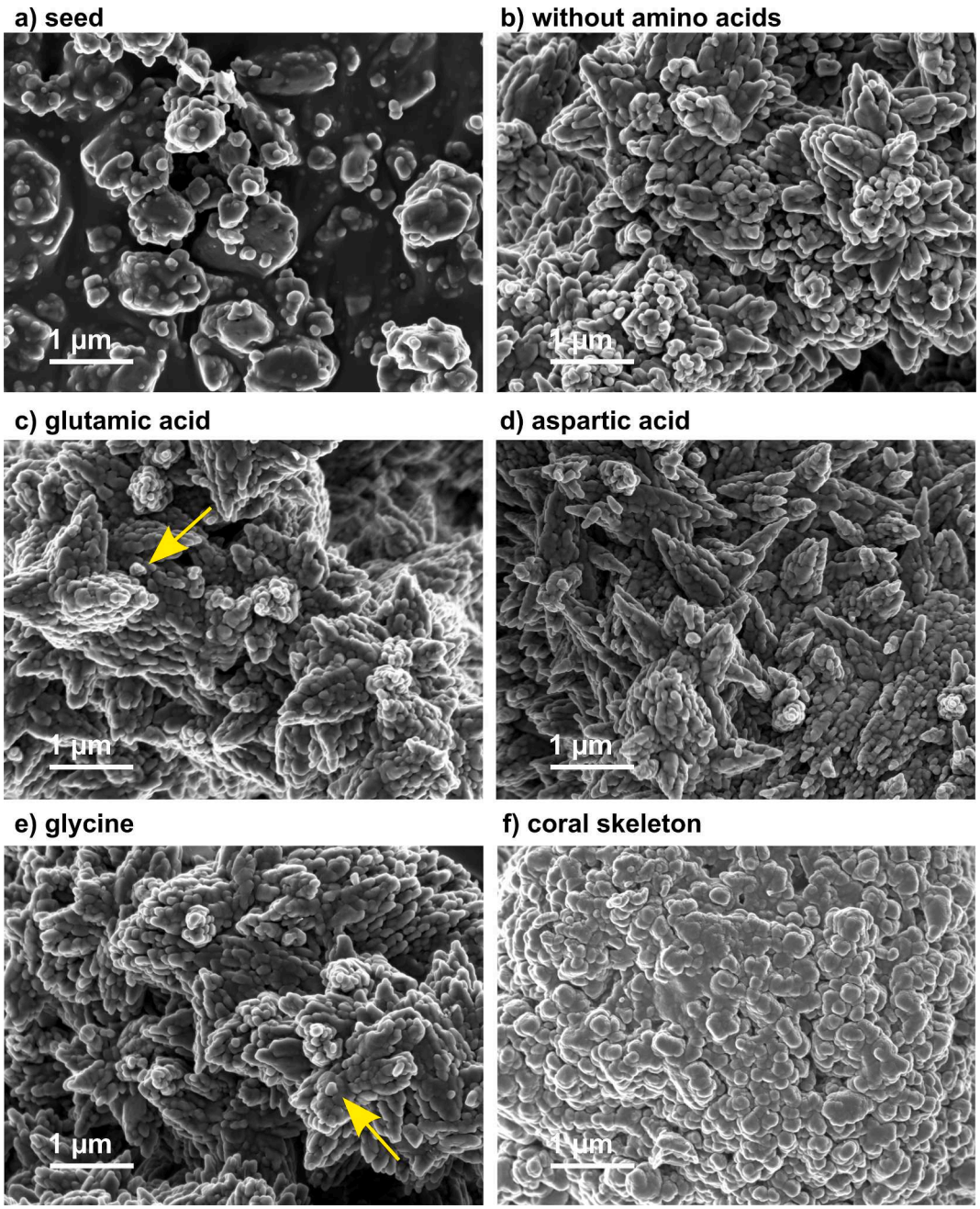

Fig. 8. Scanning electron microscopy images of a) the aragonite seed, and of precipitates formed b) without amino acids, c) with glutamic acid, d) with aspartic acid and e) with glycine. f) The surface of a skeleton from a coral cultured at ~400 µatm seawater pCO_2 and 25 °C (Cole et al. 2018) is shown for comparison. All experiments were performed at $\Omega_{Ar} = 13$ and $pH_{NBS} = 8.474$ and with 2 mM of amino acid, where used. Yellow arrows indicate studs on the pyramidal crystals.

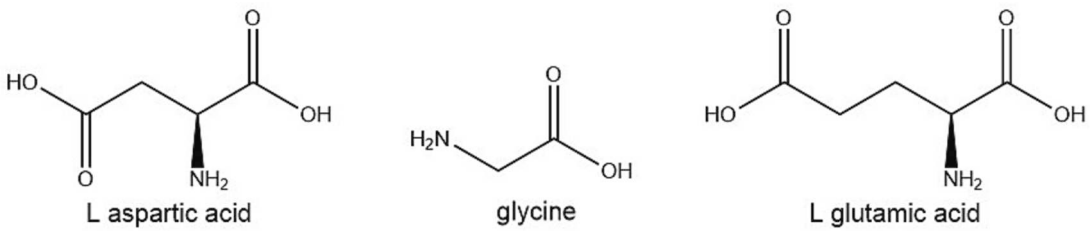

Fig. 9. Chemical structures of the amino acids used in this study.

nano-particles typically 100–200 nm in dimensions. The radiating pyramid morphology suggests that aragonite nucleates on the surface of the seed, extends to form pyramids but is ultimately obscured by fresh aragonite nucleating onto these existing pyramids. Fresh nucleation appears as small studs on the surfaces of the pyramid crystals (yellow arrows in Fig. 8).

We observe changes in the surface morphology of aragonite precipitated in the presence of aspartic acid with the pyramid crystals becoming pointier with the addition of this amino acid (as reported by Kellock et al., 2022). This provides evidence that aspartic acid causes a shift in the precipitation mechanism, rather than slowing or hindering a single process, as may be the case with the glutamic and glycine additives which create precipitates with similar morphology to the control. Additives can influence crystal morphology by adsorbing to the crystal surface and blocking mineral growth, or by being incorporated into the crystal, creating defects which influence crystal habit (Thompson et al., 2004; Shtukenberg et al., 2017). This suggests that the biomolecule is stabilising (or hindering growth on) particular crystal faces and forcing crystal propagation to move to other, less favoured surfaces.

The surface crystal morphologies observed here are markedly different from the elongate needle or fibre-like aragonites reported in many other synthetic aragonite studies (e.g. Holcomb et al., 2009; Mavromatis et al., 2015). Seawater Ω_{Ar} was not controlled during the Holcomb et al (2009) study and Ω_{Ar} reduced from 12 to 44 at the start of each precipitation to 2 to 4 at the end (Holcomb et al., 2009). Mavromatis et al., (2015) precipitated aragonites in NaCl solutions with low Ω_{Ar} (1.3 to 4.5). In both these studies the aragonite surfaces viewed by SEM must have been deposited at low Ω_{Ar}. Fibre morphologies were also observed when aragonite was formed during diffusion of ammonium carbonate into Ca-bearing solutions (Sun et al., 2017). Ω_{Ar} was not constrained in this last study but is likely to have been low. Aragonites precipitated by mixing Na_2CO_3 and $CaCl_2$ solutions changed from exhibiting needle morphology to flake morphology as reactant molarity increased (Chakrabarty and Mahapatra, 1999). Collectively these studies suggest that aragonite needle morphology is observed at low Ω_{Ar}. Morphology may change at higher Ω (Chakrabarty and Mahapatra, 1999) or due to the addition of additives (e.g. Willinger et al., 2015). In addition, confinement may alter crystal morphology if space for crystal growth is limited to one direction (Willinger et al., 2015). Further microscopy of precipitates produced at constant Ω_{Ar} (within each titration) and spanning a range of Ω (between titrations) is required to fully identify relationships between crystal habit and Ω and to idenitfy how the presence of other ions and organic additives influences crystal morphology (Falini et al., 2009).

The morphologies of the synthetic aragonite crystals precipitated in the present study at $\Omega_{Ar} = 13$ (close to the saturation state of the extracellular coral calcification media, Sevilgen et al., 2019) are also markedly different from the crystal habits typically observed in coral skeletons (Wells 1956; Holcomb et al., 2009; Drake et al., 2020). The bulk of coral skeletons are composed of elongate crystal fibres which appear similar to some synthetic aragonites (Holcomb et al., 2009). Coral skeleton surfaces typically exhibit approximately circular (potentially pseudo-hexagonal) nano particles up to ~200 nm in diameter (Fig. 8f and von Euw et al., 2017). The freshly nucleated studs observed in the synthetic aragonites in the present study are not observed on the coral skeleton surface. Rather aragonite growth occurs by extension of the existing crystals into space in a direction perpendicular to the skeletal surface i.e. out of the page in Fig. 8f. Similar morphology is observed in some mollusc nacre (Gao et al., 2019). Further research is required to explore why the aragonites produced in the present study do not resemble coral skeletal crystals despite the similarity in precipitating fluid Ω. Although fibrous synthetic aragonites duplicate the crystal morphology of coral skeletal fibres, the full width half maxima of the Raman aragonite v_1 peak, an indicator of rotational disorder in the aragonite structure, is higher in fibrous synthetic aragonites compared to shallow and deep-water corals (Farfan et al., 2022). This indicates that variations in crystallography can still exist even when synthetic and biogenic aragonites appear morphologically similar.

4.4. Implications for biomineralization

Our study shows that $[HCO_3^-]$ has no significant effect on aragonite precipitation rate in seawater over a broad range of Ω_{Ar}, relevant to biomineralizing organisms. This clarifies one route whereby ocean acidification reduces calcification rates in aragonitic marine organisms including corals (Williamson and Turley, 2012). Calcareous organisms usually produce their $CaCO_3$ minerals at specialist calcification sites and increase the pH of the calcification media to promote mineral formation (Al Horani et al., 2003; Liu et al., 2020). This pH increase shifts the dissolved inorganic carbon (DIC) equilibria to favour the speciation of CO_3^{2-} at the expense of HCO_3^- (and CO_2) and also creates a concentration gradient promoting the diffusion of CO_2 into the media (Erez, 1978). This acts as a DIC concentration mechanism (Erez, 1978) and increases the concentrations of both HCO_3^- and CO_3^{2-} at the calcification site. To date it has been unclear if ocean acidification reduces calcification because 1) both CO_3^{2-} and HCO_3^- are involved in $CaCO_3$ precipitation and are reduced in concentration due to suppression of the DIC concentration mechanism at lower pH or 2) only CO_3^{2-} is involved in $CaCO_3$ formation and is reduced in concentration due to both suppression of the DIC concentration mechanism and the influence of pH on the relative proportion of CO_3^{2-} in the calcification media. The present study suggests that only CO_3^{2-} is involved in aragonite precipitation and that the latter scenario contributes to reduced calcification under ocean acidification.

Under future climate scenarios both seawater temperatures and pCO_2 are predicted to increase (Pörtner et al., 2019). In addition, corals cultured under ocean acidification scenarios have higher concentrations of skeletal organics (Tambutté et al., 2015; Coronado et al., 2019) and amino acids (Kellock et al., 2020). All amino acids in this study inhibit aragonite precipitation, and increasing amino acid concentration either results in greater or similar inhibition (Fig. 3). Decreasing seawater Ω_{Ar} (as likely occurs under decreased calcification media pH) also increases amino acid inhibition of aragonite precipitation (Fig. 5) but increasing seawater temperature decreases inhibition by aspartic acid and mitigates this effect.

We estimate the potential effects of each of these factors on aragonite precipitation. The extracellular coral calcification media has a Ω_{Ar} of ~11 (Sevilgen et al., 2019) and decreasing this to 8 (consistent with a decrease in calcification media of 0.08 pH units at constant media pCO_2) will inhibit aragonite precipitation by ~10 % of the rate observed at $\Omega_A = 11$ (assuming an aspartic acid concentration of 2 mM, Fig. 5). Increasing seawater pCO_2 from 400 to 750 μatm raised the aspartic acid concentrations of *Porites* spp. coral skeleton by 35 %, on average (Kellock et al., 2020). The aspartic acid concentration at the calcification site is unknown but an increase in the amino acid concentration of this magnitude is typically associated with a drop in aragonite precipitation rate of <10 % (Fig. 3). Increasing seawater temperature from 25 to 27 °C accelerates aragonite precipitation rates both with and without 1 mM aspartic acid by about 30 %. This estimation suggests that the acceleration of aragonite precipitation by increasing seawater temperatures will more than offset the predicted decreases in precipitation due to inhibition of aragonite precipitation by increased skeletal aspartic acid and reduced calcification media Ω_{Ar}. This calculation is based on abiogenic observations and does not take into effect the deleterious impact of temperature rise above the coral temperature stress threshold. Our experiments provide valuable information on the interaction of amino acids with aragonite precipitation over a range of biologically relevant Ω_{Ar} and temperatures, and yield insights into how biomolecules may influence skeletal formation in a changing climate.

5. Conclusions

We explored controls on aragonite precipitation rates over a broad range of Ω_{Ar} conditions including those likely to occur in tropical coral calcification media. We find that fluid Ω_{Ar} or $[CO_3^{2-}]$ is the main control on aragonite precipitation rate from seawater at 25 °C, with no significant contributions from HCO_3^- or pH. Aspartic acid, glutamic acid and glycine at 0.2 to 5 mM all decrease aragonite precipitation rates at 25 °C. Aspartic acid (2 mM), the only amino acid tested over a temperature range, inhibited aragonite precipitation from 10 to 30 °C and also altered the morphology of the aragonite overgrowths. In all cases higher inhibition was observed in the experiments with the lowest aragonite precipitation rates i.e. at low Ω in experiments with all the amino acids at 25 °C and at low temperatures with aspartic acid. This may reflect enhanced incorporation of the amino acids in aragonite at low aragonite precipitation rates. Reduced coral calcification site Ω_{Ar} and increased aspartic acid (as likely occurs in corals in response to ocean acidification) decrease aragonite precipitation rates but this can be offset by increases in seawater temperature.

Declaration of competing interest

The authors declare that they have no known competing financial interests or personal relationships that could have appeared to influence the work reported in this paper.

Acknowledgements

This work was supported by the UK Natural Environment Research Council (NE/S001417/1) to NA, KP, RK, MC and AF. We thank Gavin Peters, University of St Andrews, for assistance with BET analyses. Electron microscopy was carried out in the Aberdeen Centre for Electron Microscopy, Analysis and Characterisation (ACEMAC).

Research Data

Data are available through Mendeley Data at https://data.mendeley.com/datasets/b5bpfw97cg/1.

Appendix A. Supplementary material

Supplementary material to this article can be found online at https://doi.org/10.1016/j.gca.2023.10.032.

References

Addadi, L., Weiner, S., 1985. Interactions between acidic proteins and crystals: stereochemical requirements in biomineralization. Proc. Natl. Acad. Sci. U.S.A. 82, 4110–4114.
Al-Horani, F.A., Al-Moghrabi, S.M., De Beer, D., 2003. The mechanism of calcification and its relation to photosynthesis and respiration in the scleractinian coral *Galaxea fascicularis*. Mar. Biol. 142, 419–426.
Allison, N., Cole, C., Hintz, C., Hintz, K., Rae, J., Finch, A., 2018. The effect of ocean acidification on tropical coral calcification: insights from calcification fluid DIC chemistry. Chem. Geol. 497, 162–169.
Allison, N., Cole, C., Hintz, C., Hintz, K., Rae, J., Finch, A., 2021. Resolving the interactions of ocean acidification and temperature on coral calcification media pH. Coral Reefs 40, 1807–1818.
Andersson, M.P., Rodriguez-Blanco, J.D., Stipp, S.L.S., 2016. Is bicarbonate stable in and on the calcite surface? Geochim. Cosmochim. Acta 176, 198–205.
Beck, R., Seiersten, M., Andreassen, J.P., 2013. The constant composition method for crystallization of calcium carbonate at constant supersaturation. J. Cryst. Growth 380, 187–196.
Berner, R.A., 1975. The role of magnesium in the crystal growth of calcite and aragonite from sea water. Geochim. Cosmochim. Acta 39, 489–504.
Borelli, G., Mayer-Gostan, N., Merle, P.L., De Pontual, H., Boeuf, G., Allemand, D., Payan, P., 2003. Composition of biomineral organic matrices with special emphasis on turbot (*Psetta maxima*) otolith and endolymph. Calcif. Tissue Int. 72, 717–725.
Brunauer, S., Emmett, P.H., Teller, E., 1938. Adsorption of gases in multimolecular layers. J. Am. Chem. Soc. 60, 309–319.
Burton, E.A., Walter, L.M., 1987. Relative precipitation rates of aragonite and Mg calcite from seawater: temperature or carbonate ion control? Geology 15, 111–114.
Chakrabarty, D., Mahapatra, S., 1999. Aragonite crystals with unconventional morphologies. J. Mater. Chem. 9, 2953–2957.
Christoffersen, J., Christoffersen, M.R., 1990. Kinetics of spiral growth of calcite crystals and determination of the absolute rate constant. J. Cryst. Growth 100, 203–211.
Cole, C., Finch, A., Hintz, C., Hintz, K., Allison, N., 2016. Understanding cold bias: variable response of skeletal Sr/Ca to seawater pCO_2 in acclimated massive *Porites* corals. Sci. Rep. 6, 26888.
Cole, C., Finch, A.A., Hintz, C., Hintz, K., Allison, N., 2018. Effects of seawater pCO_2 and temperature on calcification and productivity in the coral genus *Porites* spp.: an exploration of potential interaction mechanisms. Coral Reefs 37, 471–481.
Coronado, I., Fine, W., Bosellini, F.R., Stolarski, J., 2019. Impact of ocean acidification on crystallographic vital effect of the coral skeleton. Nat. Comm. 10, 1–9.
Cuif, J.P., Dauphin, Y., Berthet, P., Jegoudez, J., 2004. Water and organic compounds in coral skeletons: quantitative thermogravimetry coupled to infrared absorption spectrometry. Geochem. Geophys. Geosyst. 5, 11.
Cuif, J.P., Dauphin, Y., Farre, B., Nehrke, G., Nouet, J., Salomé, M., 2008. Distribution of sulphated polysaccharides within calcareous biominerals suggests a widely shared two-step crystallization process for the microstructural growth units. Mineral. Mag. 72, 233–237.
Dauphin, Y., 2006. Structure and composition of the septal nacreous layer of *Nautilus macromphalus* L. (Mollusca, Cephalopoda). Zool. 109, 85–95.
De Carlo, T.M., 2018. Characterizing coral skeleton mineralogy with Raman spectroscopy. Nat. Comm. 9, 5325.
De Carlo, T.M., Gaetani, G.A., Holcomb, M., Cohen, A.L., 2015. Experimental determination of factors controlling U/Ca of aragonite precipitated from seawater: implications for interpreting coral skeleton. Geochim. Cosmochim. Acta 162, 151–165.
De Carlo, T.M., D'Olivo, J.P., Foster, T., Holcomb, M., Becker, T., McCulloch, M.T., 2017. Coral calcifying fluid aragonite saturation states derived from Raman spectroscopy. Biogeosciences 14, 5253–5269.
De Carlo, T.M., Holcomb, M., McCulloch, M.T., 2018. Reviews and syntheses: revisiting the boron systematics of aragonite and their application to coral calcification. Biogeosciences 15, 2819–2834.
De Stefano, C., Foti, C., Gianguzza, A., Rigano, C., Sammartano, S., 1995. Chemical speciation of amino acids in electrolyte solutions containing major components of natural fluids. Chem. Spec. Bioavailab. 7, 1–8.
de Yoreo, J.J., Vekilov, P.G., 2003. Principles of crystal nucleation and growth. Rev. Mineral. Geochem. 54, 57–93.
Dickson, A.G., 1990. Standard potential of the reaction: $AgCl(s) + 12H_2(g) = Ag(s) + HCl(aq)$, and and the standard acidity constant of the ion HSO_4^- in synthetic sea water from 273.15 to 318.15 K. J. Chem. Thermodyn. 22, 113–127.
Drake, J.L., Mass, T., Stolarski, J., Von Euw, S., van de Schootbrugge, B., Falkowski, P.G., 2020. How corals made rocks through the ages. Glob. Chang. Biol. 26, 31–53.
Elhadj, S., De Yoreo, J.J., Hoyer, J.R., Dove, P.M., 2006. Role of molecular charge and hydrophilicity in regulating the kinetics of crystal growth. PNAS 103, 19237–19242.
Erez, J., 1978. Vital effect on stable-isotope composition seen in foraminifera and coral skeletons. Nature 273, 199–202.
Falini, G., Fermani, S., Tosi, G., Dinelli, E., 2009. Calcium carbonate morphology and structure in the presence of seawater ions and humic acids. Cryst. Growth Des. 9 (5), 2065–2072.
Fang, Y., Lee, S., Xu, H., Farfan, G.A., 2023. Organic controls over biomineral Ca–Mg carbonate compositions and morphologies. Cryst. Growth Des. 23, 4872–4882.
Farfan, G.A., Apprill, A., Cohen, A., DeCarlo, T.M., Post, J.E., Waller, R.G., Hansel, C.M., 2022. Crystallographic and chemical signatures in coral skeletal aragonite. Coral Reefs 41, 19–34.
Finch, A.A., Allison, N., Sutton, S.R., Newville, M., 2003. Strontium in coral aragonite: 1. Characterization of Sr coordination by extended absorption X-ray fine structure. Geochim. Cosmochim. Acta 67, 1197–1202.
Finney, A.R., Innocenti, M.R., Freeman, C.L., Harding, J.H., 2020. Amino acid and oligopeptide effects on calcium carbonate solutions. Cryst. Growth Des. 20, 3077–3092.
Gao, R., Wang, R., Feng, X., Zhang, G., 2019. Growth of nacre biocrystals by self-assembly of aragonite nanoparticles with novel subhedral morphology. Crystals 10, 3.
Gebauer, D., Cölfen, H., Verch, A., Antonietti, M., 2009. The multiple roles of additives in $CaCO_3$ crystallization: a quantitative case study. Adv. Mater. 21, 435–439.
Gilbert, P.U.P.A., Abrecht, M., Frazer, B.H., 2018. The organic-mineral interface in biominerals, In: *Molecular Geomicrobiology*, Reviews in Mineralogy and Geochemistry, Mineralogical Society of America, pp. 157–186.
Guo, S., Ward, M.D., Wesson, J.A., 2002. Direct visualization of calcium oxalate monohydrate crystallization and dissolution with atomic force microscopy and the role of polymeric additives. Langmuir 18, 4284–4291.
Holcomb, M., Cohen, A.L., Gabitov, R.I., Hutter, J.L., 2009. Compositional and morphological features of aragonite precipitated experimentally from seawater and biogenically by corals. Geochim. Cosmochim. Acta 73, 4166–4179.
Holcomb, M., Venn, A.A., Tambutté, E., Tambutté, S., Allemand, D., Trotter, J., McCulloch, M., 2014. Coral calcifying fluid pH dictates response to ocean acidification. Sci. Rep. 4.
Holcomb, M., DeCarlo, T.M., Gaetani, G.A., McCulloch, M., 2016. Factors affecting B/Ca ratios in synthetic aragonite. Chem. Geol. 437, 67–76.
Jung, T., Kim, W.-S., Kyun Choi, C., 2005. Crystal structure and morphology control of calcium oxalate using biopolymeric additives in crystallization. J. Cryst. Growth 279, 154–162.
Kawano, M., Tokonami, M., 2014. Synthesis of calcite and aragonite, and quantitative evaluation of amino acid adsorption on their surfaces. Clay Sci. 18, 33–41.

Kellermeier, M., Rosenberg, R., Moise, A., Anders, U., Przybylski, M., Cölfen, H., 2012. Amino acids form prenucleation clusters: ESI-MS as a fast detection method in comparison to analytical ultracentrifugation. Faraday Discuss. 159, 23–45.
Kellock, C., Cole, C., Penkman, K., Evans, D., Kröger, R., Hintz, C., Hintz, K., Finch, A., Allison, N., 2020. The role of aspartic acid in reducing coral calcification under ocean acidification conditions. Sci. Rep. 10, 12797.
Kellock, C., Castillo Alvarez, M.C., Finch, A., Penkman, K., Kröger, R., Clog, M., Allison, N., 2022. Optimising a method for aragonite precipitation in simulated biogenic calcification media. PLoS One 17, e0278627.
Lee, K., Kim, T.W., Byrne, R.H., Millero, F.J., Feely, R.A., Liu, Y.M., 2010. The universal ratio of boron to chlorinity for the North Pacific and North Atlantic oceans. Geochim. Cosmochim. Acta 74, 1801–1811.
Lemke, T., Edte, M., Gebauer, D., Peter, C., 2021. Three reasons why aspartic acid and glutamic acid sequences have a surprisingly different influence on mineralization. J. Phys. Chem. B 125, 10335–10343.
Liu, Y.W., Sutton, J.N., Ries, J.B., Eagle, R.A., 2020. Regulation of calcification site pH is a polyphyletic but not always governing response to ocean acidification. Sci. Adv. 6, eaax1314.
Lueker, T.J., Dickson, A.G., Keeling, C.D., 2000. Ocean pCO_2 calculated from dissolved inorganic carbon, alkalinity, and equations for K_1 and K_2: validation based on laboratory measurements of CO_2 in gas and seawater at equilibrium. Mar. Chem. 70, 105–119.
Mavromatis, V., Montouillout, V., Noireaux, J., Gaillardet, J., Schott, J., 2015. Characterization of boron incorporation and speciation in calcite and aragonite from co-precipitation experiments under controlled pH, temperature and precipitation rate. Geochim. Cosmochim. Acta 150, 299–313.
Millero, F.J., 2013. Chemical Oceanography, fourth ed.
Montanari, G., Lakshtanov, L.Z., Tobler, D.J., Dideriksen, K., Dalby, K.N., Bovet, N., Stipp, S.L.S., 2016. Effect of aspartic acid and glycine on calcite growth. Cryst. Growth Des. 16, 4813–4821.
Morse, J.W., Arvidson, R.S., Lüttge, A., 2007. Calcium carbonate formation and dissolution. Chem. Rev. 107, 342–381.
Mucci, A., 1983. The solubility of calcite and aragonite in seawater at various salinities, temperatures, and one atmosphere total pressure. Am. J. Sci. 283, 780–799.
Mucci, A., Morse, J.W., 1984. The solubility of calcite in seawater solutions of various magnesium concentration, It = 0.697 m at 25 °C and one atmosphere total pressure. Geochim Cosmochim. Acta 48, 815–822.
Nielsen, L.C., de Yoreo, J.J., DePaolo, D.J., 2013. General model for calcite growth kinetics in the presence of impurity ions. Geochim. Cosmochim. Acta 115, 100–114.
Pan, Y., Li, Y., Ma, Q., He, H., Wang, S., Sun, Z., Cai, W.J., Dong, B., Di, Y., Fu, W., Chen, C.T.A., 2021. The role of Mg^{2+} in inhibiting $CaCO_3$ precipitation from seawater. Mar. Chem. 237, 104036.
Picker, A., Kellermeier, M., Seto, J., Gebauer, D., Cölfen, H., 2012. The multiple effects of amino acids on the early stages of calcium carbonate crystallization. Zeitschrift Für Kristallographie-Crystalline Materials 227, 744–757.
Pierrot, D., Lewis, E.D., Wallace, W.R., 2006. MS Excel Program Developed for CO_2 System Calculations. Oak Ridge National Laboratory.
Pörtner, H.-O., Roberts, D.C., Masson-Delmotte, V., Zhai, P., Tignor, M., Poloczanska, E., Mintenbeck, K., Nicolai, M., Okem, A., Petzold, J., Ram, B., Weyer, N., 2019. The ocean and cryosphere in a changing climate. IPCC special report on the ocean and cryosphere in a changing climate, 1155.
Rahman, M.A., Shinjo, R., Oomori, T., Wörheide, G., 2013. Analysis of the proteinaceous components of the organic matrix of calcitic sclerites from the soft coral *Sinularia* sp. PLoS One 8.
Sand, K.K., Tobler, D.J., Dobberschütz, S., Larsen, K.K., Makovicky, E., Andersson, M.P., Wolthers, M., Stipp, S.L.S., 2016. Calcite growth kinetics: dependence on saturation index, Ca^{2+}:CO_3^{2-} activity ratio, and surface atomic structure. Cryst. Growth Des. 16, 3602–3612.
Sevilgen, D.S., Venn, A.A., Hu, M.Y., Tambutté, E., de Beer, D., Planas-Bielsa, V., Tambutté, S., 2019. Full in vivo characterization of carbonate chemistry at the site of calcification in corals. Sci. Adv. 5, eaau7447.
Shtukenberg, A.G., Ward, M.D., Kahr, B., 2017. Crystal growth with macromolecular additives. Chem. Rev. 117, 14042–14090.
Sikirić, M.D., Füredi-Milhofer, H., 2006. The influence of surface active molecules on the crystallization of biominerals in solution. Adv. Colloid Interface Sci. 128, 135–158.
Stepić, R., Jurković, L., Klementyeva, K., Ukrainczyk, M., Gredičak, M., Smith, D.M., Kralj, D., Smith, A.S., 2020. Adsorption of aspartate derivatives to calcite surfaces in aqueous environment. Cryst. Growth Des. 20, 2853–2859.
Sun, C.Y., Marcus, M.A., Frazier, M.J., Giuffre, A.J., Mass, T., Gilbert, P.U.P.A., 2017. Spherulitic growth of coral skeletons and synthetic aragonite: nature's three-dimensional printing. ACS Nano 11, 6612–6622.
Sun, C.Y., Stifler, C.A., Chopdekar, R.V., Schmidt, C.A., Parida, G., Schoeppler, V., Fordyce, B.I., Brau, J.H., Mass, T., Tambutté, S., Gilbert, P.U.P.A., 2020. From particle attachment to space-filling coral skeletons. Proc. Natl. Acad. Sci. U.S.A. 117, 30159–30170.
Suzuki, M., Saruwatari, K., Kogure, T., Yamamoto, Y., Nishimura, T., Kato, T., Nagasawa, H., 2009. An acidic matrix protein, Pif, is a key macromolecule for nacre formation. Science 325, 1388–1390.
Takeuchi, T., Sarashina, I., Iijima, M., Endo, K., 2008. *In vitro* regulation of $CaCO_3$ crystal polymorphism by the highly acidic molluscan shell protein Aspein. FEBS Lett. 582, 591–596.
Tambutté, E., Venn, A.A., Holcomb, M., Segonds, N., Techer, N., Zoccola, D., Allemand, D., Tambutté, S., 2015. Morphological plasticity of the coral skeleton under CO_2-driven seawater acidification. Nat. Commun. 6, 7368.
Thompson, C., Davies, M.C., Roberts, C.J., Tendler, S.J., Wilkinson, M.J., 2004. The effects of additives on the growth and morphology of paracetamol (acetaminophen) crystals. Int. J. Pharm. 280, 137–150.
Urmos, J., Mackenzie, F.T., Sharma, S.K., 1991. Characterizations of some biogenic carbonates with Raman spectroscopy. Am. Mineral. 76, 641–646.
Van der Weijden, R.D., Van Der Heijden, A.E., Witkamp, G.J., Van Rosmalen, G.M., 1997. The influence of total calcium and total carbonate on the growth rate of calcite. J. Cryst. Growth 171, 190–196.
van der Weijden, C.H., van der Weijden, R.D., 2014. Calcite growth: rate dependence on saturation, on ratios of dissolved calcium and (bi)carbonate and on their complexes. J. Crys.t Growth 394, 137–144.
Venn, A.A., Tambutté, E., Holcomb, M., Laurent, J., Allemand, D., Tambutté, S., 2013. Impact of seawater acidification on pH at the tissue-skeleton interface and calcification in reef corals. Proc. Natl. Acad. Sci. U.S.A. 110, 1634–1639.
Venn, A.A., Tambutté, E., Caminiti-Segonds, N., Techer, N., Allemand, D., Tambutté, S., 2019. Effects of light and darkness on pH regulation in three coral species exposed to seawater acidification. Sci. Rep. 9, 1–12.
Venn, A.A., Tambutté, E., Comeau, S., Tambutté, S., 2022. Proton gradients across the coral calcifying cell layer: effects of light, ocean acidification and carbonate chemistry. Front. Mar. Sci. 9, 973908.
von Euw, S., Zhang, Q., Manichev, V., Murali, N., Gross, J., Feldman, L.C., Gustafsson, T., Flach, C., Mendelsohn, R., Falkowski, P.G., 2017. Biological control of aragonite formation in stony corals. Science 356, 933–938.
Weiner, S., 1979. Aspartic acid-rich proteins: major components of the soluble organic matrix of mollusk shells. Calcif. Tissue Int. 29, 163–167.
Weiner, S., Addadi, L., 1991. Acidic macromolecules of mineralized tissues: the controllers of crystal formation. Trends Biochem Sci. 16, 252–256.
Wells, J.W., 1956. Scleractinia. In: Moore, R.C. (Ed.), Treatise on Invertebrate Paleontology, Part F Coelenterata. Univ. of Kansas Press, Lawrence, pp. 328–444.
Williamson, P., Turley, C., 2012. Ocean acidification in a geoengineering context. Philos. Trans. R. Soc. A 370, 4317–4342.
Willinger, M.G., Polleux, J., Antonietti, M., Cölfen, H., Pinna, N., Nassif, N., 2015. Structural evolution of aragonite superstructures obtained in the presence of the siderophore deferoxamine. CrstEngComm 17, 3927–3935.
Wolf, S.E., Loges, N., Mathiasch, B., Panthöfer, M., Mey, I., Janshoff, A., Tremel, W., 2007. Phase selection of calcium carbonate through the chirality of adsorbed amino acids. Angew. Chem. Int. Ed. Engl. 46, 5618–5623.
Wolthers, M., Nehrke, G., Gustafsson, J.P., van Cappellen, P., 2012. Calcite growth kinetics: modeling the effect of solution stoichiometry. Geochim. Cosmochim. Acta 77, 121–134.